Radiative cooling of two-component wire-array Z-pinch plasma

V. V. Ivanov, R. C. Mancini, D. Papp, P. Hakel, T. Durmaz, and R. Florido

View Online   **Export Citation**   **CrossMark**

ARTICLES YOU MAY BE INTERESTED IN

Multiple-view spectrally resolved x-ray imaging observations of polar-direct-drive implosions on OMEGA
Physics of Plasmas **21**, 122704 (2014); https://doi.org/10.1063/1.4903324

Compressed shell conditions extracted from spectroscopic analysis of Ti K-shell absorption spectra with evaluation of line self-emission
Physics of Plasmas **21**, 082711 (2014); https://doi.org/10.1063/1.4892554

Radiative cooling of two-component wire-array Z-pinch plasma

V. V. Ivanov,[1] R. C. Mancini,[1] D. Papp,[1] P. Hakel,[1,a)] T. Durmaz,[1] and R. Florido[1,2]
[1]*Department of Physics, University of Nevada, Reno, Nevada 89557, USA*
[2]*Departamento de Física, Universidad de Las Palmas de Gran Canaria, 35017 Las Palmas de Gran Canaria, Spain*

Wire-array two-component Z-pinch plasmas containing Al and other elements were studied experimentally and the observations interpreted with the help of theoretical modeling. Special attention was given to achieving reproducible implosions. Cascading implosions in star wire arrays mix components during the implosion phase and implosion dynamics were not affected by changes in concentration. A reduction in Al K-shell radiation and an increase in soft x-ray radiation emission were observed in Al-W plasma with 84% concentration of Al ions compared to only-Al plasma. Plasma with 84% of Al ions has radiative properties like those of W Z-pinches. The analysis of Al K-shell x-ray spectra with a collisional-radiative atomic kinetics model shows a drop of the electron temperature from 400 eV in pure Al plasma to below 300 eV in the Al-W mix. Al-Au Z-pinches present radiation features similar to Al-W plasma. This is indicative of a similar plasma cooling effect due to the presence of a high-Z element. © 2014 AIP Publishing LLC.
[http://dx.doi.org/10.1063/1.4892180]

I. INTRODUCTION

Wire-array Z-pinches are presently the most powerful laboratory source of x-ray radiation in the soft and keV ranges.[1–3] The mixing of two elements in the Z-pinch can change radiative properties of plasma.[4] Al-Mg wire arrays have demonstrated enhanced x-ray yield in the keV photon energy range because of the smaller opacity of Z-pinch plasmas.[5] In this connection, study of two-component plasmas provides new opportunities to control the radiative properties of Z-pinches. Achieving homogeneous and reproducible mixing of different components in the Z-pinch plays a crucial role in this study. While many materials are not available as an alloy combination that can be used to produce thin wires, wires of different materials can be placed together in the same wire array. Indeed, two-component cylindrical, double-nested, and planar wire arrays were studied for implosion dynamics, x-ray yields, and for developing spectroscopic analysis methods.[5–9] Implosion of mixed wire arrays depends strongly on the location and mass of wires of different elements in the array. In cylindrical arrays, two-step implosions are observed in two-component loads. Double nested multi-wire arrays operate in "a transparent mode" when material from the external cylindrical array passes through the inner cylinder during the implosion.[10] The numbers of wires may be different in the inner and external cylinders. All these features make the implosion dynamics of two-component arrays complicated. In addition, formation of the precursor also adds complexity to the plasma dynamics because the subsequent implosion onto the precursor can form a multi-layer pinch. If one changes the balance of elements in cylindrical and nested wire arrays by varying the wire diameters or numbers; then, the implosion dynamics and x-ray yield can be affected.[11]

Star and planar wire arrays in a 1 MA machine can have another implosion dynamics, with cascading from wire to wire to the center of the load.[12,13] The cascading mitigates the bubble-like implosion instability[14,15] and leads to a more homogeneous Z-pinch. The regime of cascading depends on the distribution of mass in the wires and on the location of different components.

In this paper, we report on experiments that were carried out with two-component star and planar wire-array Z-pinches. The location of wires with different masses and materials was optimized to provide reproducible mixing of different components during the cascade implosion. We found a strong dependence of the x-ray emission from these two-component wire arrays on the concentration of components.

II. EXPERIMENTAL SETUP AND MEASUREMENTS

The experiments discussed in this paper were carried out on the Zebra generator with a 1-MA current pulse and a rising edge of 80 ns (10%–90%). Laser diagnostics include five-frame probing of the Z-pinch with a wavelength of 532 nm along three directions, and one frame at 266 nm. Short-duration 150-ps probing pulses with wavelengths of 532 nm and 266 nm provided high-contrast images of the fast imploding plasma.[16,17] Optical plasma diagnostics include a time-gated CCD camera and a streak camera. Temporal profiles of x-ray pulses were recorded with filtered x-ray diodes (XRD) and photo-conducting detectors (PCD). Total radiating energy was measured with a bare Ni bolometer in the spectral region from 10 eV to 4–5 keV. The power of the x-ray pulse was calculated from the XRD with a 2–μm Kimfol filter normalized to Ni bolometer yield. The electron temperature and density of Z-pinch plasmas were extracted from the analysis of time-integrated, axially resolved Al K-shell line spectra. Spectra in the range $\lambda = 5$–10 Å were recorded

---

a)Current address: Los Alamos National Laboratory, NM 87545, USA.

by an x-ray spectrometer equipped with a convex KAP crystal on x-ray film and spectral resolution of $\lambda/\delta\lambda \sim 350$.[16] The width of the spectrometer slit was varied from 0.05 to 1.5 mm to optimize intensity of x-ray radiation from two-component plasma on the film. A time-gated pinhole camera recorded 6 frames in two spectral regions with frame duration of 3–4 ns. The experiments were carried out with 2 cm tall 9-wire star wire-arrays with masses between m = 42–45 μg/cm and linear 6- and 8-wire arrays with m = 80–90 μg/cm. We tested wire arrays with Al as the first component (pure Al or alloy with 5% of Mg). Several materials were used for the second component: W, Ti, stainless steel (SS) alloy, and Au. Concentration of two elements was varied by variation of wire diameters but total mass of loads was constant.

Star and linear wire arrays were used to provide homogeneous mixing of elements in cascade implosion. Experiments had showed that distributions of current in mixed arrays can differ from their distributions in mono-material loads.[18] A cascading regime is not established in wire-arrays with non-optimal location and masses of wires. Figure 1 presents a shadowgram of implosion in Ti-Al 8-wire linear array with Ti wire on edges and Al wires near the center. Laser probing with a wavelength of 266 nm shows fine details of wire-array implosions at the 1-MA Zebra machine.[17] The implosion began with edge Ti wires because of the high j × B force and fast ablation on edge wires. The beginning of the implosion of the edge wires is typical for mono-element star and linear arrays.[12,13] Whereas the implosion in mono-element wire-arrays cascades from wire to wire to the center of the load, Figure 1 presents another type of implosion. Near-center Al wires began to implode along with edge Ti wires. This implosion is disorganized because Ti and Al plasmas reach the center at different times. The cascading regime is observed if we swap positions of Al and Ti wires in the array. The wire-array with Al wires located on the edge and Ti wires placed near the center implodes with cascading. We compared the x-ray yield and power
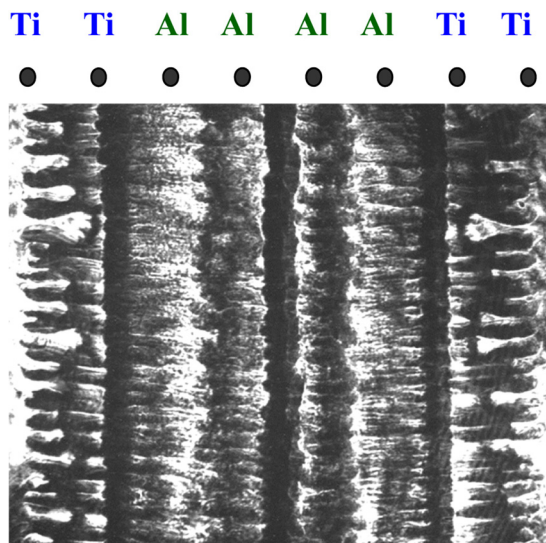
from two 8-wire linear arrays with same masses but different locations of Al and Ti wires.

Implosions with cascading dynamics produce 45% higher x-ray power and 60% higher x-ray energy of Al K-shell emission compared to disorganized implosion. We conjecture that cascading mixes the imploding plasma and produces a reproducible multi-component Z-pinch plasma. The following empirical rule was used to design wire-arrays that generate cascading in two-component arrays: wire mass and atomic number of wire element increase or remain constant from the edge to the center of the array. Figure 2(b) presents a cascade implosion in Al-W three-ray star with W wires in the inner cylinder [see a top view on the load in (a)]. The arrow points to the bubble of imploding Al plasma from wires (4, 5), which pushes W wire (3) on the inner cylinder. It is seen that W wires remain on their initial position during collision and start to implode later along with the Al plasma and reach the center at the same time. Three-ray stars with diameters 16/12/5 mm operate in the non-precursor regime when plasma does not ablate to the center of the array in the ablation phase.[13,19] The concentration of components in the Z-pinch can be varied by adjusting the wire diameters; this does not affect the implosion dynamics.

Series of shots were carried out with Al-W 3-ray star 9-wire arrays with different concentrations of Al ions in Al-W plasma. Figure 3 presents the total radiated energy (triangles) and energy radiated in the keV range (squares) as a function of the concentration of Al ions in the Z-pinch plasma. The total radiated energy decreases by 15% for a concentration of Al ions of 94%. Plasma with 84%–94% of Al ions emits similar amounts of total and keV x-ray energy compare to a pure W Z-pinch. Al K-shell radiation from mixed Z-pinch plasma is lower by approximately a factor of 10 compared to that of pure Al wire arrays. This indicates cooling of mixed Z-pinch plasma compared to mono-component Al Z-pinches. Diagrams (b) and (c) present x-ray pulses from XRD filtered by 2 μm Kimfol film to PCD filtered 8 μm Be foil. Diagrams show different balances of total and keV energies and widening of the XRD soft x-ray pulse in the W-doped Z pinch.
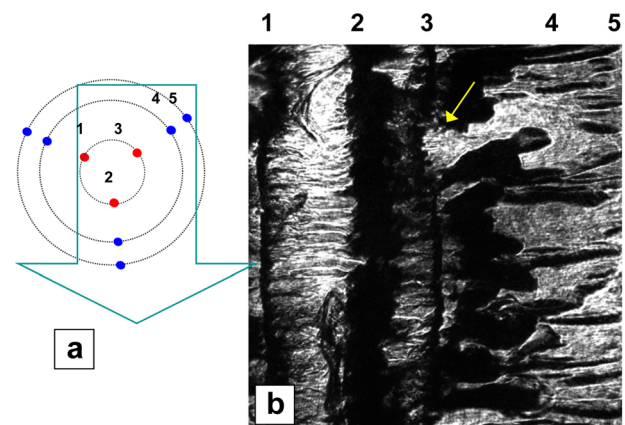

FIG. 1. The shadowgram of the 8-wire linear array with two Ti wires on the edge and two Al wires near the center, m = 83 μg/cm.

FIG. 2. (a) A top view of the star 9-wire Al-W array, Ø16/12/5 mm with W wires in the inner cylinder. An arrow shows a direction of laser probing. (b) A shadowgram of the implosion in the star wire array with a mass of 40 μg/cm.
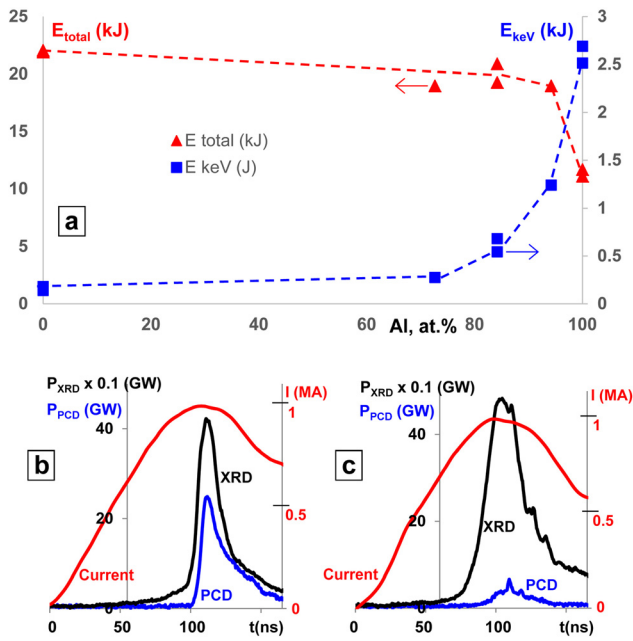
FIG. 3. (a) Diagrams for the total energy (triangles) and keV x-ray energy (squares) radiated by Al-W 3-ray 9-wire star wire arrays Ø16/12/5 mm as a function of the concentration of Al ions in plasma. Masses of star loads are between 40–45 μg/cm. (b) and (c) Current and x-ray pulses from XRD filtered by 2 μm Kimfol film and PCD with 8 μm Be foil. Diagrams are taken from the Al star load (b) and Al-W star load (c) with a concentration of Al ions of 84%.

Al-Au two-component wire arrays demonstrate similar results. Star wire arrays with 10 μm Au wires are too heavy for the 1 MA Zebra generator so these experiments were carried out with linear wire arrays. Au wire arrays demonstrated the highest radiated x-ray energy compared to other materials used in our experiments. Planar arras can generate up to 30 kJ at the Zebra generator.[20]

Al-SS two-component star wire arrays showed only small difference in total and keV energies compared to Al-W and Al-Au loads. Ti planar wire arrays showed an intermediate result between Al-Au and Al-SS loads.

Figure 4 presents the spectra from Al alloy 5056 (with 5% of Mg) arrays to two-component Al-W and Al-Au wire arrays. W, Au, and Ti Z-pinches radiate weak quasi-continuum radiation in the spectral region 5.5–8 Å. The K-shell lines of Al ions are not blended with Au or W lines and, thus, they can be used to spectroscopically determine the electron temperature and density of plasma.

III. ATOMIC MODELING AND SPECTROSCOPIC ANALYSIS

In order to extract conditions in the plasma, we have analyzed the Al line emission spectra with a theoretical spectral model. This model consists of several building blocks: (1) a collisional-radiative atomic-kinetics model for Al plasmas, (2) a calculation of emergent line intensity distribution including spectroscopic-quality radiation transport, and (3) an
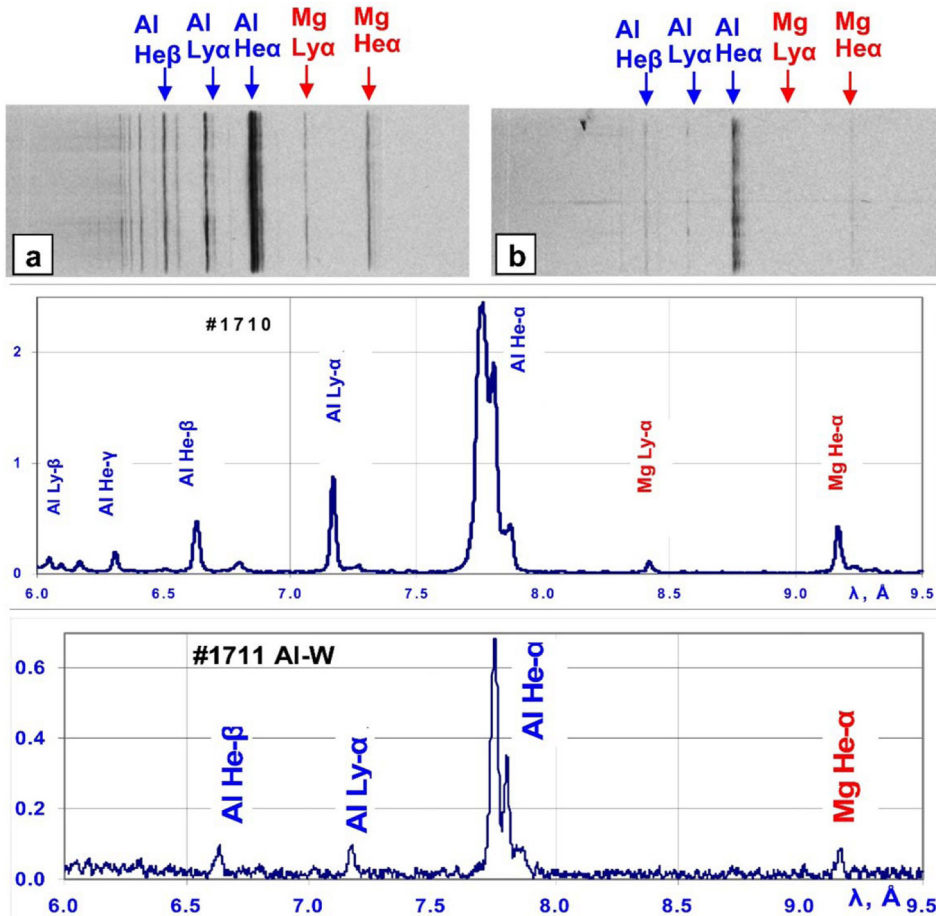

FIG. 4. X-ray spectra and the corresponding plots for shots #1710 (Al/Mg) and #1711 (Al/W).

automated search and optimization procedure for finding the best match between the synthetic and experimental spectra. We focus on the photon-energy range of 1800 eV–2160 eV (5.74 A–6.89 A) that includes the Al lines with the smallest optical depth, namely, the He-like series 1s np → 1s^2 starting with Heβ (n = 3), their Li-like satellite transitions, and the Lyβ line (3p → 1s) from the H-like Al ion.

For a pair of electron temperature T_e and ion number density N_{ion}, we calculate the steady-state NLTE populations of Al states with the code ABAKO[21] by solving a system of atomic kinetic rate equations

$$A \cdot N = 0, \qquad (1)$$

where A is the rate matrix and N is the vector of atomic level populations. Rates for the following atomic processes are taken into account: electron collisional excitation and deexcitation, electron collisional ionization, three-body and radiative recombination, spontaneous radiative decay, autoionization, and electron capture. Radiation transport effects on the level population kinetics are approximated with escape factors using formulae appropriate for cylindrical geometry.[22] The level populations are then used to compute the photon-energy dependent emissivity and opacity of the plasma for a range of temperature and density values, namely, 100 eV to 700 eV in electron temperature T_e and Al ion number density N_{ion} (ions/cm^3) from 5×10^{17} to 1×10^{22}. The energy level structure includes up to 1616 levels: the fully stripped ion, 100 levels in H-like Al, 352 levels in He-like Al, 519 levels in Li-like Al, and 644 levels in Be-like Al.

The photon-energy-dependent emissivities j_ν and opacities k_ν are given by[23]

$$j_\nu = \sum_i \sum_{j<i} N_i A_{ij} \Phi_{ij}(\nu) \frac{h\nu}{4\pi}, \qquad (2a)$$

$$k_\nu = \sum_i \sum_{j<i} (N_j B_{ji} - N_i B_{ij}) \Phi_{ij}(\nu) \frac{h\nu}{4\pi}, \qquad (2b)$$

where Φ represents Voigt line shapes associated with transitions between atomic bound states i and j. Here, we invoke the complete redistribution approximation in which the absorption and emission line shapes are identical. The Voigt line shapes account for natural and Doppler broadening

effects. The symbols A_{ij}, B_{ij}, and B_{ji} stand for the Einstein coefficients for spontaneous and stimulated emission, and absorption. We have also constructed a similar but independent Al database using the HULLAC suite of atomic codes.[24] The processing and results from this kinetic model are similar to those based on ABAKO.

Given the emissivity and opacity, we then calculate the emergent intensity distribution by integrating the radiation transport equation along chords in the plasma source. The line-of-sight is perpendicular to the Z-pinch plasma axis. This integration takes into account line overlapping effects. In this model, the radius of the pinch is a parameter, which we estimate to be in the range of $r = 0.45$–0.90 mm based on the laser shadowgrams of the pinch. Before comparing with the data, the synthetic spectrum is convolved with a Gaussian function to account for the finite resolution power of the spectrometer (i.e., instrumental broadening), which, in this case, represents the dominant broadening effect.

For the experiments discussed here, the aluminum ions are highly ionized with an average ionization of ~11, and the population distribution is dominated by He-like and H-like Al ions. The spectroscopy diagnosis relies on the analysis of K-shell line spectrum. The relative intensity distribution of this spectrum is sensitive to variations in plasma electron temperature and density through the temperature and density sensitivity of the atomic level population kinetics. In order to illustrate the temperature sensitivity, in Fig. 5, we show the computed Al emission spectrum at a representative atom density of $N_{ion} = 2 \times 10^{19}$ cm^{-3} for three different T_e values. The photon energy ranges from 1800 to 2100 eV. Characteristic Al K-shell resonance line transitions in the spectrum include Heβ1s3p→1s^2, Heγ1s4p→1s^2, Heδ1s5p→1s^2, Heε1s6p→1s^2, and Lyβ3p→1s, as well as their satellite lines in Li-like and He-like ions. As temperature increases, the ionization balance shifts to higher ionized atoms. Within the same ion stage, relative intensities of resonance lines remain almost unchanged (we note that, in Fig. 5, the intensity distribution is Heβ-normalized, so that the computed spectrum actually shows the intensity of each line relative to that of Heβ). However, the intensity ratio of same type of lines in different ionization stages is very sensitive to T_e: as seen in Fig. 5, the intensity ratio of Lyβ to Heβ increases with temperature. Also, the temperature dependence of a satellite to parent line ratio decreases with
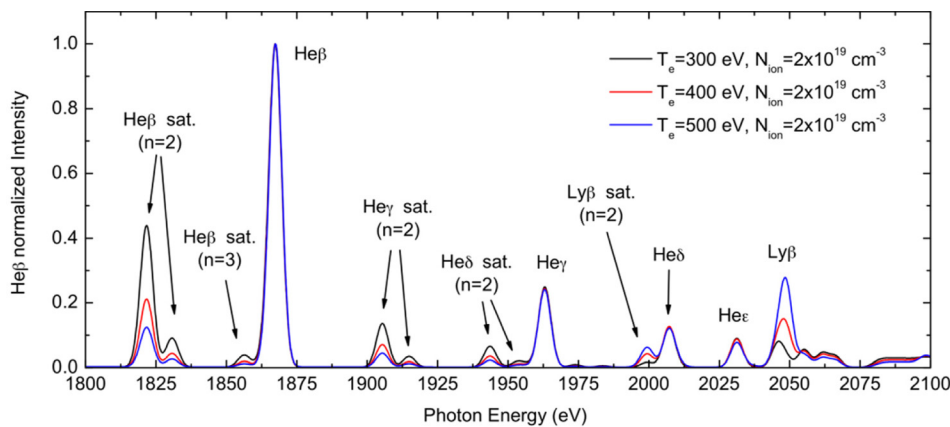

FIG. 5. Electron temperature sensitivity of the Al K-shell spectrum in the 1800 eV–2100 eV photon energy range.
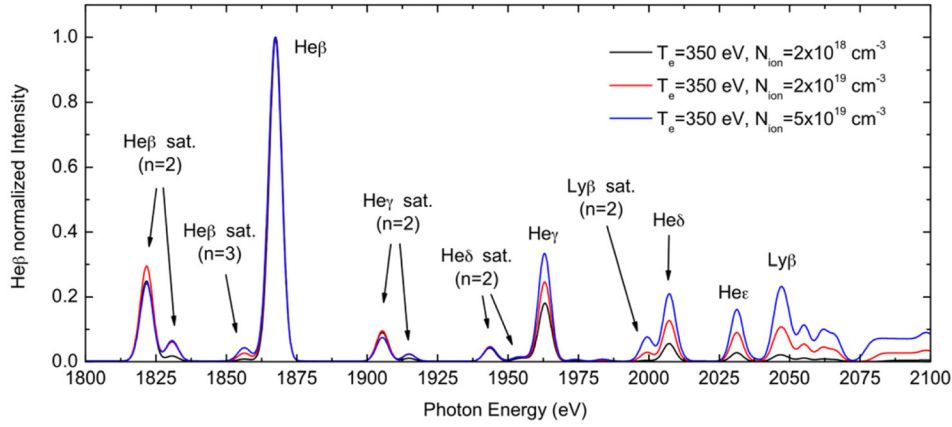
FIG. 6. Electron density sensitivity of the Al K-shell spectrum in the 1800 eV–2100 eV photon energy range.

increasing temperature. This effect can be observed in Fig. 5, where several Li-like satellites and one He-like satellite of He-like and H-like resonance lines, respectively, have been labeled. Hence, relative line intensities across three ionization stages are employed to extract T_e from the data.

In dense plasmas, the density diagnosis usually relies on the analysis of Stark-broadened line shapes, which strongly depend on density. But, the density conditions achieved in the Z-pinch Al plasmas discussed here are not large enough for the Stark effect to be significant. In fact, instrumental broadening dominates the width of the lines. In the present case, the density sensitivity in the emission spectrum arises from the density dependence of the ionization balance in the range of conditions for these Al plasmas and, particularly, by the effect of three-body recombination on the distribution of atomic level populations. This density sensitivity is illustrated in Fig. 6, where we show the Al emission spectrum for three different N_{ion} values at a constant $T_e = 350$ eV. Within the density range of interest, the average ionization increases with density. This is a characteristic behavior of the collisional-radiative atomic kinetics of plasmas at moderate densities. As the electron density increases, the collisional excitation becomes more important, thus, populating the excited states. These, in turn, can undergo electron impact ionization, which finally leads to an increase in average ionization.[21] For $T_e = 350$ eV and an ion density of $N_{ion} = 2 \times 10^{18}$ cm^{-3}, the average ionization of the Al plasma is $\langle Z \rangle = 11$; for $N_{ion} = 2 \times 10^{19}$ cm^{-3}, $\langle Z \rangle = 11.2$; and for $N_{ion} = 5 \times 10^{19}$ cm^{-3}, $\langle Z \rangle = 11.4$. This behavior also

manifests in the Al emission spectrum (see Fig. 6) as an enhancement of the Lyβ/Heβ intensity ratio as the density increases. Satellite lines remain now quite insensitive to density changes but, important for diagnosis purposes, the relative intensity distribution of the series of He-like line transitions $1s^2$–$1s$ np changes with density. The larger the n the larger the relative increase in intensity.

This effect is the result of how the three-body recombination affects the atomic level population distribution. At these densities, this atomic process (whose rate scales with N_e^2) begins to impact the population distribution by transferring population from H-like ground state to He-like highly excited states, since the three-body recombination preferentially populates excited states. In order to confirm this behavior, we artificially set the three-body recombination rate to zero in the ABAKO model, and recomputed level populations and the emergent intensity distribution. The results are shown in Fig. 7. As density goes up, an increase of Lyβ/Heβ intensity ratio is still observed (as discussed above, mainly due to the collisional excitation plus collisional ionization two-step mechanism). Nevertheless, by neglecting the three-body recombination, the density sensitivity of He-like series lines is lost. In this case, the average ionization of the Al plasma is $\langle Z \rangle = 11.0$, 11.2, and 11.5 for $N_{ion} = 2 \times 10^{18}$, 2×10^{19}, and 5×10^{19} cm^{-3}, respectively, at a constant temperature of $T_e = 350$ eV. Compared to full atomic kinetics calculations, we see that the three-body recombination has a small impact on the overall ionization balance but it produces a density-dependent population distribution in the
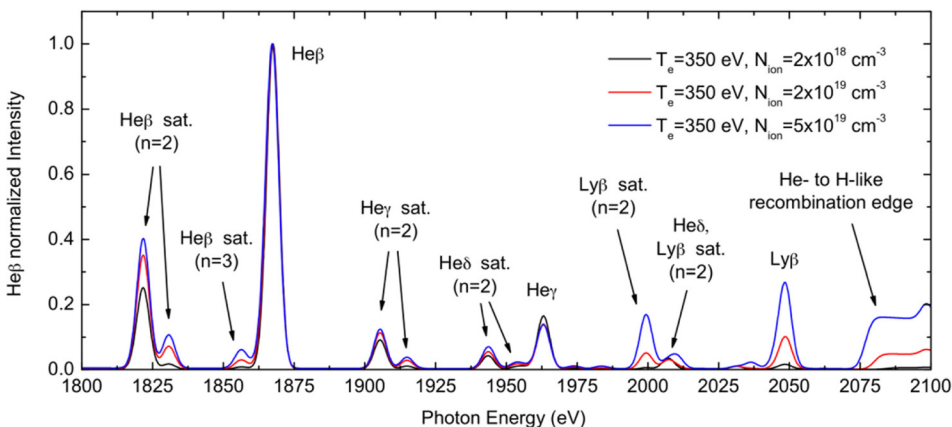

FIG. 7. Al K-shell spectrum calculated for the same conditions of Fig. 6 but now not including the three-body recombination process in the calculation of the level population atomic kinetics.

excited state of He-like Al, which impacts the emission spectrum by altering the relative intensity of the series He-like lines arising from those excited states. We note in passing that, to the best of our knowledge, this density-sensitivity has not been previously employed for plasma density diagnosis.

The characteristic electron temperature and atom density of the Z-pinch plasma are estimated by finding the pair of values whose associated synthetic spectrum produces the best agreement with the observed spectra. This is accomplished by performing an exhaustive search across the temperature and density parameter space for the smallest Q^2 defined as

$$Q^2 = \sum_{p=1}^{N} w_p [I_p^{th}(T, N_A) - c I_p^{ex}]^2. \tag{3}$$

The parameter c is responsible for unit conversion between the experimental and theoretical spectral line intensities and is determined during the automated search procedure. Before the calculation, the experimental spectrum is cleared of background estimated from experimental signal from regions with no lines. Also, the photon-energy axis of the experimental spectrum is recalibrated so that its line positions coincide with the theoretical values. This recalibration results in line shifts of at most a few eV and is necessary in order to have an optimally defined Q^2. The weight factors w_p are estimated automatically during the search from the noise in the experimental data assuming Poisson statistics[25] and relate to the uncertainty ε_p at each point $p = h\nu_p$ as

$$w_p = \frac{1}{\varepsilon_p^2}. \tag{4}$$

Locating the global minimum of the weighted Q^2 produces estimates of the temperature and density of the plasma. We further determine the statistical uncertainties of temperature and density from the local curvature of the Q^2 surface around this minimum.[25–27] Using second-order finite-difference formulae, we calculate the second derivatives of Q^2 with respect to T and N_{ion} at this global minimum and use them to construct the curvature matrix $\boldsymbol{\alpha}$

$$\alpha = \frac{1}{2} \begin{pmatrix} \dfrac{\partial^2 Q^2}{\partial T^2} & \dfrac{\partial^2 Q^2}{\partial T \partial N_A} \\ \dfrac{\partial^2 Q^2}{\partial N_A \partial T} & \dfrac{\partial^2 Q^2}{\partial N_A^2} \end{pmatrix}. \tag{5}$$

The standard deviations for temperature and density are then determined from the diagonal elements of the covariance matrix $C = \alpha^{-1}$

$$\sigma_T = \sqrt{C_{TT}}, \tag{6a}$$

$$\sigma_{N_A} = \sqrt{C_{N_A N_A}}. \tag{6b}$$

The quality of the best fit can be assessed by inspecting the value of the "normalized" Q^2 (denoted NQ^2), which is defined as

$$NQ^2 = \frac{Q^2}{N - M}, \tag{7}$$

where N is the number of data points included in the definition of Q^2 and M is the number of fit parameters. In our case, N is of the order of several hundred and $M = 2$ (the fit parameters are the temperature and density). A "good" fit is characterized by values of $NQ^2 \sim 1$.

IV. RESULTS

We have analyzed the Al spectra recorded during several different wire array shots. These were shots #1710 (Al-Mg Alloy 5056), #1734 (pure Al), #1724 (Al/Ti), #1730 (Al/SS), and #1712 (Al/W). Assuming a radius of r = 0.45 mm for the Z-pinch plasma, the analysis results are displayed in Table I.

Changing the value of the pinch radius used in the analysis to its upper-bound value of r = 0.90 mm does not significantly affect the inferred temperature and density conditions. The fitting was performed by minimizing Q^2 over two photon-energy ranges: 1800–1880 eV and 1950–2060 eV. This covers all lines starting from the Li-like satellites of the Heβ on the low-energy end of the range and ending with the Lyβ located near the He-like series limit (see Fig. 8). The region between the Heβ and Heγ lines has no prominent spectral features.

The statistical uncertainties inferred from the curvature of the Q^2 surface are consistently less than the spacing used in the temperature and density grids that discretize the parameter space. Therefore, the estimated errors are determined by the grid step. In temperature, this leads to uncertainty value ± 20 eV. In density, we have uncertainties up to 50% of the optimum (Q^2-minimizing) value. In general, we see that the best fit found by the automated Q^2-minimization procedure follows the experimental spectrum within its uncertainty band (ε_p); so in that sense, it is a successful fit. This is supported by the resulting NQ^2 values, which are all close to the ideal value of 1 (see Table I), which is a rigorous criterion for the quality and success of the theoretical fit to the experimental data. The Q^2 surface plots reveal the challenging characteristics of this analysis. The global minima are located in long shallow valleys elongated along a direction that is oblique to both the temperature and density axes. This means that in addition to the global minimum producing a successful theoretical fit to the experimental data, there is always a collection of temperature-density pairs that result in fits that are also quite good. This makes the results sensitive to the details of the actual form of the Q^2 function, i.e., what spectral regions are included in its definition. The orientation of this valley is such that a good fit can also be obtained by selecting a lower

TABLE I. Characteristic temperature and density values, their statistical uncertainties, and the normalized Q^2.

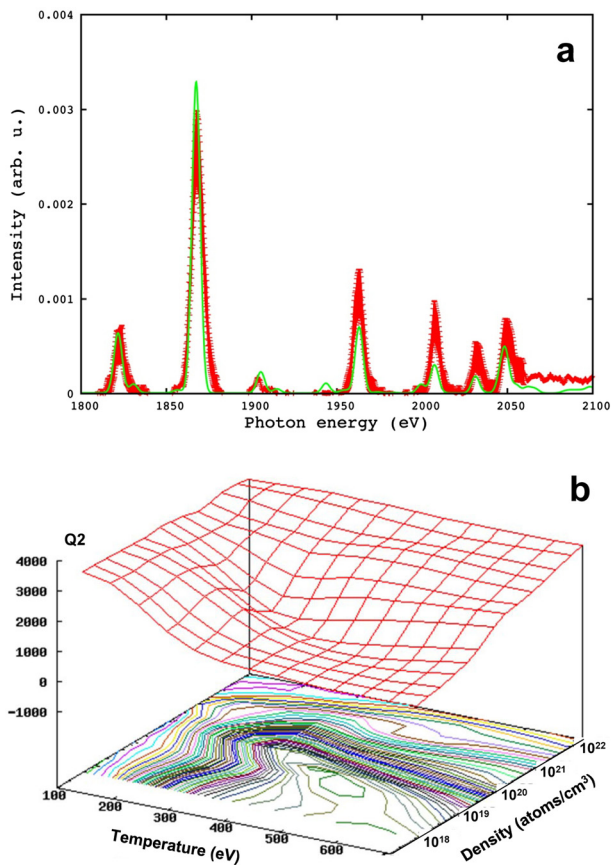|	T (eV)	N_A (at./cm^3)	NQ^2
#1710 (Al/Mg)	400 ± 20	$(2 \pm 0.3) \times 10^{19}$	0.88
#1734 (Al)	450 ± 20	$(1 \pm 0.1) \times 10^{19}$	1.48
#1724 (Al/Ti)	350 ± 20	$(1 \pm 0.1) \times 10^{20}$	1.34
#1730 (Al/SS)	400 ± 20	$(5 \pm 0.6) \times 10^{19}$	1.44
#1712 (Al/W)	< 300		

FIG. 8. Shot #1734: (a) The experimental spectrum with computed error bars (red) and the "best-fit" synthetic spectrum (green); (b) the Q^2 surface plot with the minimum reached at $T = 450$ eV, $N_A = 1 \times 10^{19}$ atoms/cm^3.

density combined with a higher temperature. The inherent limitations of our current model and analysis are linked to the fact that we assign an effective temperature and density to a dynamically developing plasma using spectra that are time- and, partly, space-integrated, i.e., we use a uniform plasma model. The Al/W case was not suited for a formal analysis using our automated procedure since it only showed hints of the Heβ and Heγ lines and no other lines. Even so, this allows us to conclude that, in this case, the temperature of the plasma was noticeably lower than in the other shots. From an inspection of the visible lines using a custom-made collisional-radiative model of the mixed Al/W plasma, we estimate it to be less than 300 eV. This case, compared to the other shots, clearly demonstrates the cooling effect that the presence of a high-Z element such as W have on the temperature of the plasma. The spectra from the Al/Au plasma were similar to this Al/W case in that they were also indicative of lower temperatures.

V. CONCLUSIONS

We have experimentally studied wire-array Z-pinches composed of several different chemical elements and analyzed the measurements with x-ray line emission spectroscopy. We observed that mixed Al-W wire arrays Z-pinch plasmas with 16% of W radiate in a manner similar to a 100% W Z-pinch. Spectra from mixed plasma show a drop of Al K-shell radiation and an increase of soft x-ray radiation compared to the case of 100% Al plasma. Modeling and analysis of Al K-shell x-ray spectra with collisional-radiative atomic kinetics models show the effect of the radiative cooling in the Al-W plasma. For the experiments discussed here, the typical duration of the assembly, stagnation, and radiation emission phase of the pinch plasma is 10–20 ns. These times are larger than the radiative cooling times of the plasma (estimated as the ratio of the density of internal energy to density of radiated power[23]) which, for the cases in Table I, are less than 1 ns: in the range of hundreds of picoseconds. Also, radiative cooling times are affected by the presence of a higher atomic number element in the plasma. For example, the radiative cooling time for the Al/Ti plasma in Table I is 21% shorter than the Al plasma at the same conditions. And, for the Al/W case is 45% shorter than the Al plasma at the same conditions. Two-component Al-Au Z-pinches present radiation features similar to Al-W plasma. We conclude that the radiative properties of two-component star wire arrays can be controlled with the choice and the variation of concentration of components.

[1]C. Deeney, R. Douglas, R. B. Spielman, T. J. Nash, D. L. Peterson, P. L'Eplattenier, G. A. Chandler, J. F. Seaman, and K. W. Struve, Phys. Rev. Lett. **81**, 4883 (1998).
[2]M. E. Cuneo, E. M. Waisman, S. V. Lebedev, J. P. Chittenden, W. A. Stygar, G. A. Chandler, R. A. Vesey, E. P. Yu, T. J. Nash, D. E. Bliss, G. S. Sarkisov *et al.*, Phys. Rev. E **71**, 046406 (2005).
[3]C. A. Coverdale, C. Deeney, B. Jones, J. W. Thornhill, K. G. Whitney, A. L. Velikovich, R. W. Clark, Y. K. Chong, J. P. Apruzese, J. Davis, and P. D. LePell, IEEE Trans. Plasma Sci. **35**, 582 (2007).
[4]J. P. Apruzese and J. Davis, J. Appl. Phys. **57**, 4349 (1985).
[5]C. Deeney, P. D. LePell, B. H. Failor, S. l. Wong, J. P. Apruzese, K. G. Whitney, J. W. Thornhill, J. Davis, E. Yadlonsky, R. C. Hazelton *et al.*, Phys. Rev. E **51**, 4823 (1995).
[6]S. V. Lebedev, F. N. Beg, S. N. Bland, J. P. Chittenden, A. E. Dangor, and M. G. Haines, Phys. Plasmas **9**, 2293 (2002).
[7]K. M. Williamson, V. L. Kantsyrev, A. A. Esaulov, A. S. Safronova, N. D. Ouart, F. M. Yilmaz, I. K. Shrestha, V. Shlyaptseva, R. D. McBride, D. A. Chalenski *et al.*, Phys. Plasmas **16**, 012704 (2009).
[8]V. L. Kantsyrev, L. I. Rudakov, A. S. Safronova, A. A. Esaulov, A. S. Chuvatin, C. A. Coverdale, C. Deeney, K. M. Williamson, M. F. Yilmaz, I. Shrestha *et al.*, Phys. Plasmas **15**, 030704 (2008).
[9]B. Jones, C. Deeney, C. A. Coverdale, P. D. LePell, J. L. McKenney, J. P. Apruzese, J. W. Thornhill, K. G. Whitney, R. W. Clark, A. L. Velikovich *et al.*, J. Quant. Spectrosc. Radiat. Transfer **99**, 341 (2006).
[10]M. E. Cuneo, D. B. Sinars, D. E. Bliss, E. M. Waisman, J. L. Porter, W. A. Stygar, S. V. Lebedev, J. P. Chittenden, G. S. Sarkisov, and B. B. Afeyan *et al.*, Phys. Rev. Lett. **94**, 225003 (2005).
[11]C. A. Coverdale, C. Jennings, B. Jones, M. E. Cuneo, and C. Deeney, Bull. Am. Phys. Soc. **55**(15), 245 (2010).
[12]V. V. Ivanov, V. I. Sotnikov, A. Haboub, G. E. Sarkisov, R. Presura, and T. E. Cowan, Phys. Plasmas **14**, 032703 (2007).
[13]V. V. Ivanov, V. I. Sotnikov, A. Haboub, A. P. Shevelko, A. L. Astanovitskiy, A. Morozov, E. D. Kazakov, and S. D. Altemara, Phys. Rev. Lett. **100**, 025004 (2008).
[14]S. V. Lebedev, D. J. Ampleford, S. N. Bland *et al.*, Plasma Phys. Controlled Fusion **47**, A91 (2005).
[15]V. V. Ivanov, V. I. Sotnikov, G. S. Sarkisov, T. E. Cowan, S. N. Bland, B. Jones, C. A. Coverdale, C. Deeney, P. J. Laca, A. L. Astanovitskiy, and A. Haboub, Phys. Rev. Lett. **97**, 125001 (2006).

[16]V. V. Ivanov, V. I. Sotnikov, J. M. Kindel, P. Hakel, R. C. Mancini, A. L. Astanovitskiy, A. Haboub, S. D. Altemara, A. P. Shevelko, E. D. Kazakov, and P. V. Sasorov, Phys. Rev. E **79**, 056404 (2009).

[17]V. V. Ivanov, J. P. Chittenden, S. D. Altemara, N. Niasse, P. Hakel, R. C. Mancini, D. Papp, and A. A. Anderson, Phys. Rev. Lett. **107**, 165002 (2011).

[18]V. V. Ivanov, A. L. Astanovitskiy, D. Papp, J. P. Chittenden, S. N. Bland, B. Jones, and S. D. Altemara, Phys. Plasmas **17**, 102702 (2010).

[19]D. Papp, V. V. Ivanov, B. Jones, A. Haboub, A. A. Anderson, S. D. Altemara, and B. R. Talbot, Phys. Plasmas **19**, 092704 (2012).

[20]A. S. Safronova, A. A. Esaulov, V. L. Kantsyrev, N. D. Ouart, V. Shlyaptseva, M. E. Weller, S. F. Keim, K. M. Williamson, I. Shrestha, and G. C. Osborne, High Energy Density Phys. **7**, 252 (2011).

[21]R. Florido, R. Rodríguez, J. M. Gil, J. G. Rubiano, P. Martel, D. Suarez, M. Mendoza, and E. Mínguez, J. Phys. Conf. Ser. **112**, 042008 (2008).

[22]R. C. Mancini, R. F. Joyce, and C. F. Hooper, Jr., J. Phys. B **20**, 2975 (1987).

[23]D. Mihalas and B. Weibel-Mihalas, *Foundations of Radiation Hydrodynamics* (Dover Publications, Mineola, New York, 1999).

[24]A. Bar-Shalom, M. Klapisch, and J. Oreg, J. Quant. Spectrosc. Radiat. Transfer **71**, 169 (2001).

[25]R. Coldwell and G. J. Bamford, *Theory and Operation of Spectral Analysis Using ROBFIT* (Springer-Verlag, New York, 1995).

[26]W. Press, S. A. Teukolsky, W. T. Vetterling, and B. P. Flannery, *Numerical Recipes*, 3rd ed. (Cambridge University Press, 2007).

[27]P. R. Bevington and D. K. Robinson, *Data Reduction and Error Analysis for the Physical Sciences*, 3rd ed. (McGraw-Hill, New York, 2002).